Blind Compressed Sensing Enables 3-Dimensional Dynamic Free Breathing Magnetic Resonance Imaging of Lung Volumes and Diaphragm Motion

Sampada Bhave, MS, Sajan Goud Lingala, PhD,† John D. Newell Jr, MD,‡§ Scott K. Nagle, MD, PhD,‖ and Mathews Jacob, PhD**

Objectives: The objective of this study was to increase the spatial and temporal resolution of dynamic 3-dimensional (3D) magnetic resonance imaging (MRI) of lung volumes and diaphragm motion. To achieve this goal, we evaluate the utility of the proposed blind compressed sensing (BCS) algorithm to recover data from highly undersampled measurements.

Materials and Methods: We evaluated the performance of the BCS scheme to recover dynamic data sets from retrospectively and prospectively undersampled measurements. We also compared its performance against that of view-sharing, the nuclear norm minimization scheme, and the l_1 Fourier sparsity regularization scheme. Quantitative experiments were performed on a healthy subject using a fully sampled 2D data set with uniform radial sampling, which was retrospectively undersampled with 16 radial spokes per frame to correspond to an undersampling factor of 8. The images obtained from the 4 reconstruction schemes were compared with the fully sampled data using mean square error and normalized high-frequency error metrics. The schemes were also compared using prospective 3D data acquired on a Siemens 3 T TIM TRIO MRI scanner on 8 healthy subjects during free breathing. Two expert cardiothoracic radiologists (R1 and R2) qualitatively evaluated the reconstructed 3D data sets using a 5-point scale (0-4) on the basis of spatial resolution, temporal resolution, and presence of aliasing artifacts.

Results: The BCS scheme gives better reconstructions (mean square error = 0.0232 and normalized high frequency = 0.133) than the other schemes in the 2D retrospective undersampling experiments, producing minimally distorted reconstructions up to an acceleration factor of 8 (16 radial spokes per frame). The prospective 3D experiments show that the BCS scheme provides visually improved reconstructions than the other schemes do. The BCS scheme provides improved qualitative scores over nuclear norm and l_1 Fourier sparsity regularization schemes in the temporal blurring and spatial blurring categories. The qualitative scores for aliasing artifacts in the images reconstructed by nuclear norm scheme and BCS scheme are comparable.

The comparisons of the tidal volume changes also show that the BCS scheme has less temporal blurring as compared with the nuclear norm minimization scheme and the l_1 Fourier sparsity regularization scheme. The minute ventilation estimated by BCS for tidal breathing in supine position (4 L/min) and the measured supine inspiratory capacity (1.5 L) is in good correlation with the literature. The improved performance of BCS can be explained by its ability to efficiently adapt to the data, thus providing a richer representation of the signal.

Conclusion: The feasibility of the BCS scheme was demonstrated for dynamic 3D free breathing MRI of lung volumes and diaphragm motion. A temporal resolution of ~500 milliseconds, spatial resolution of $2.7 \times 2.7 \times 10$ mm^3, with whole lung coverage (16 slices) was achieved using the BCS scheme.

Key Words: dynamic 3D free breathing MRI, BCS, lung volume, diaphragm motion

(*Invest Radiol* 2016;00: 00–00)

Dynamic imaging of respiratory mechanics plays an important role in the diagnosis of abnormalities to the active and passive components involved in respiratory pumping, including diaphragm paresis or paralysis, abnormal chest wall mechanics, and muscle weakness, which are a result of neuromuscular, pulmonary, or obesity-related disorders.[1,2] Clinically, these impaired respiratory mechanics are evaluated indirectly by respiratory inductive plethysmography, spirometry, or magnetometer.[3] Although these schemes can be collected with very high temporal resolution, they lack spatial information and hence can detect only global changes that occur only during the advanced stages of the disease.[4] Early detection and localization of the disease are very crucial for treatment planning.

Magnetic resonance imaging (MRI) is gaining popularity over the above techniques because it provides a noninvasive and direct visualization of dynamic changes in the diaphragm and chest wall[5–8] positions, without exposure to ionizing radiation. The evaluation of dynamic changes in lung volumes and diaphragm movement requires high spatial and temporal resolution, plus high volume coverage to cover the entire thorax. Achieving entire volume coverage is especially challenging in obese subjects who are at a high risk for impaired diaphragm movement. The respiratory rate during tidal breathing is 12 to 16 cycles per minute (~5 seconds per cycle), whereas the normal respiratory excursion of the diaphragmatic dome is about 1.5 cm.[9] The speed of the diaphragm is about 0.3 cm/s. Thus, considering a pixel size of 3×3 mm, the diaphragm position changes at a rate of 1 pixel/s. To avoid motion blurring, imaging time should be much shorter than 1 second. Although 2-dimensional (2D) imaging techniques can offer high temporal resolution, it is challenging to merge the information from multiple 2D slices for 3D visualization of the diaphragmatic dome and volume measurements because of the irregular nature of respiratory motion in most subjects.

Research has shown that 3D dynamic MRI (3D-DMRI) is a more suitable option to analyze respiratory mechanics[7,10,11] and is reported to have higher correlation with spirometry measurements than 2D-DMRI.[12] However, current 3D-DMRI implementations offer limited temporal/spatial resolution and volume coverage. Although improved resolution and coverage may be achieved by acquiring 3D volumes at multiple breath-holds, this approach does not provide good estimates of respiratory dynamics or account for the hysteresis effect that the lung exhibits during normal breathing.[1,7,9] Furthermore, subjects with chronic obstructive pulmonary disease have difficulty holding their breath, making motion analysis difficult. Fast imaging techniques were introduced for 3D-DMRI,[12–14] but current schemes still compromise on either spatial resolution or the temporal resolution. For example, echo-planar imaging–based sequences provide a temporal

Received for publication July 6, 2015; and accepted for publication, after revision, December 16, 2015.

From the *Department of Electrical and Computer Engineering, The University of Iowa; †Department of Electrical Engineering, University of Southern California, Los Angeles; Departments of ‡Radiology and §Biomedical Engineering, The University of Iowa; and ‖Department of Radiology, University of Wisconsin School of Medicine and Public Health, Wisconsin.

Reprints: Sampada Bhave, MS, Department of Electrical and Computer Engineering, 4016 Seamans Center, University of Iowa, Iowa City, IA 52242. E-mail: sampada-bhave@uiowa.edu.

Conflicts of interest and sources of funding: Grant information: NSF CCF-1116067, ACS RSG-11-267-01-CCE, and ONR N00014-13-1-0202.

The authors report no conflicts of interest.

ISSN: 0020-9996/16/0000–0000

DOI: 10.1097/RLI.0000000000000253

resolution of 330 ms/frame but can only achieve low spatial resolution[14] and partial lung coverage. Similarly, 3D fast low-angle shot (FLASH) sequences with Cartesian undersampling, view-sharing, and parallel imaging was used to obtain whole lung coverage,[12] at the expense of a poor temporal resolution of 1 second; these schemes can only be used to image the dynamics during slow and controlled breathing conditions, which limits the flexibility of experimental paradigms. More recently, higher spatiotemporal resolution was reported using a 128-channel coil array[15] with a Cartesian 3D-FLASH sequence and generalized autocalibrated partially parallel acquisition.[16] However, these custom-made 128-channel coils are not widely available, which restricts the widespread utility of this scheme.

The main focus of this work was to evaluate the feasibility of blind compressed sensing (BCS) scheme, coupled with 3D stack of stars-based golden angle radial trajectories, to enable the dynamic imaging of lung volumes and the diaphragm, with full coverage of the thorax, at the spatial and temporal resolutions needed to image tidal breathing. We compare the BCS scheme against other state-of-the-art compressed sensing schemes that model voxel profiles, such as nuclear minimization-based low rank reconstruction, l_1 Fourier sparsity-based regularization,[17–20] and the commonly used view-sharing reconstruction. We have 2 expert radiologists quantitatively score the reconstructions from all the schemes on a 4-point scale to assess diagnostic image quality.

MATERIALS AND METHODS

Image Acquisition

The institutional review board at the local institution approved all the in vivo acquisitions. All the volunteers were fully informed of the nature of the procedure and written consent was obtained. The subjects were scanned on a Siemens 3 T Trio scanner (Siemens AG, Healthcare sector, Erlangen, Germany) with a 32-channel body array coil.

For retrospectively undersampled 2D acquisition, a fully sampled 2D dynamic data set was collected on a normal subject using a gradient recalled echo sequence with uniform radial sampling pattern. The sequence parameters were as follows: field of view (FOV)-350 × 350 mm^2; slice thickness-10 mm; repetition time (TR)/echo time (TE)-2.67/1.17 milliseconds; and matrix size-128 × 128. The spatial resolution was 2.7 × 2.7 × 10 mm^3. A total of 180 frames were acquired with 256 radial spokes per frame, which resulted in a temporal resolution of 683 milliseconds.

For the prospective 3D acquisition, 8 healthy volunteers (5 men and 3 women; median age, 28 years) without any evidence of pulmonary disease were included in this study. The 3D dynamic data were collected using a FLASH sequence with a 3D radial stack of stars trajectory. The 3D acquisition uses a golden angle radial trajectory in the axial plane (k_x, k_y) combined with a conventional phase encoding step in the k_z direction. The radial spokes were separated by the golden angle (111.25°) to achieve incoherent sampling. The sequence parameters for 6 of the 8 data sets are as follows: field of view (FOV)-350 × 350 mm^2; TR/TE-2.37/0.92 milliseconds; partial Fourier factor-6/8; base matrix size-128 × 128; and spatial resolution-2.7 × 2.7 × 10 mm^3. A total of 3500 radial spokes were acquired per slice, and a total of 16 slices were acquired to obtain whole lung coverage. The data were binned by considering 16 radial spokes per frame, resulting in a temporal resolution of 492.96 ms/frame. The coil sensitivity profiles were estimated using an Eigen decomposition method.[21] The seventh data set was acquired with a larger FOV: 400 × 400 mm^2, which resulted in a slightly lower spatial resolution of 3.1 × 3.1 × 10 mm^3. All the other scan parameters were the same as those in previous acquisitions. Two data sets were collected from the eighth subject, 1 while free breathing and 1 while breathing from functional residual capacity to total lung capacity. The scan parameters for these 2 data sets were as follows: FOV-350 × 350 mm^2; TR/TE-2.37/0.92 milliseconds; base matrix size-128 × 128; spatial resolution-2.7 × 2.7 × 10 mm^3. A total of 18 slices were acquired with 3500 radial spokes per slice. 16 radial spokes were binned for each frame, which gave a temporal resolution of 683 milliseconds for these 2 data sets. The scan time for each of these data sets was less than 2 minutes.

Image Reconstruction

In this work, we pre-interpolated the radial data points on a Cartesian grid points that were within 0.5 unit of the measured sample using linear interpolation. A similar pre-interpolation step is used in constrained reconstruction algorithms for other body part applications.[17,22,23] The pre-interpolation was done for all the schemes. This enabled us to use fast Fourier transforms (FFTs) and inverse FFTs in the forward and backward models of the algorithm. There was no noticeable change in the quality of reconstructions obtained from pre-interpolated data as compared with the ones obtained from non-Cartesian data with nonuniform FFTs and inverse FFTs.

Signal Representation

The goal of the reconstruction schemes is to recover the dynamic data set $\mathbf{\Gamma}$ from its undersampled measurements. Here, $\mathbf{\Gamma}$ is an $M \times N$ Casorati matrix, where M is the number of voxels in a single timeframe and N is the number of timeframes. In other words, the columns of $\mathbf{\Gamma}$ represent the signal at every voxel. The measurements are modeled as follows:

$$b_i = \mathcal{A}_i(\Gamma) + n_i\ ;\ i = 1, \cdots, N \tag{1}$$

where b_i is the undersampled measurement and n_i is the noise for the ith timeframe. $\mathcal{A}_i = S_i F C$, where S_i is the undersampling mask, F is Fourier operator, and C is the coil sensitivity. The least squares reconstruction problem can be posed as:

$$\mathbf{\Gamma}^* = arg\,min_\Gamma \underbrace{\| \mathcal{A}(\mathbf{\Gamma}) - b \|_F^2}_{\text{Data consistency term}}. \tag{2}$$

The compressed sensing schemes considered in this article enforce different priors on the temporal profiles of the data to make the problem well posed. We discuss each of the schemes in detail below.

- Low-rank recovery using nuclear norm minimization[18–20]: This scheme assumes that the temporal profiles of pixels lie in a low-dimensional space. Figure 1a reveals the low rank structure of the data where the singular values rapidly decay to 0. The problem is formulated as a convex optimization problem given below:

$$\mathbf{\Gamma}^* = arg\,min_\Gamma \underbrace{\| \mathcal{A}(\mathbf{\Gamma}) - b \|_F^2}_{\text{Data consistency term}} + \underbrace{\lambda \| \mathbf{\Gamma} \|_*}_{\text{Nuclear norm}}, \tag{3}$$

where λ is the regularization parameter. The nuclear norm, which is a convex relaxation of the matrix rank, is defined as $\| \mathbf{\Gamma} \|_* = \sum_{i=1}^{\min\{M,N\}} \sigma_i$, where σ_i is the singular value of $\mathbf{\Gamma}$. The nuclear norm minimization scheme can be viewed as a direct alternative to classical 2-step low-rank[24] schemes, which prelearns the temporal basis functions from navigator data and uses these functions to estimate the basis images.

- l_1 Fourier sparsity regularization: This scheme exploits the sparsity of the data in the Fourier transform domain along the temporal

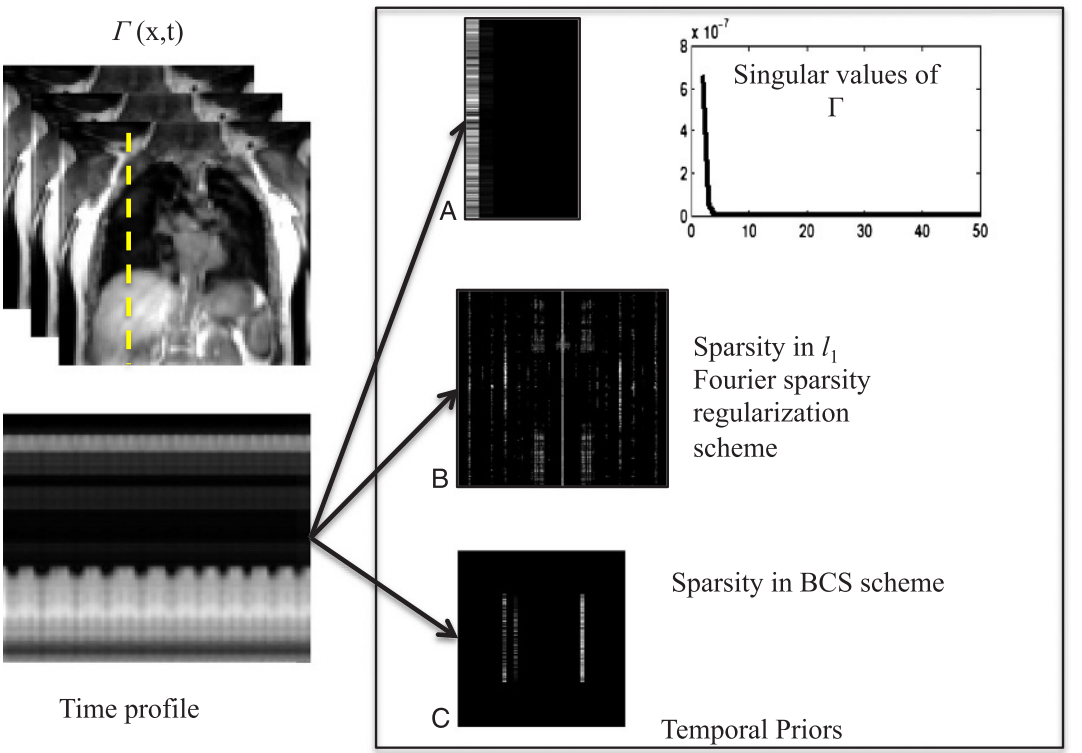

FIGURE 1. Illustration of the data representation in different transform domains: The nuclear norm minimization scheme, the l_1 Fourier sparsity regularization scheme, and the BCS scheme rely on constrained modeling of the intensity profiles of the voxels, specified by $\boldsymbol{\Gamma} = \boldsymbol{UV}$. The nuclear norm minimization scheme capitalizes on the efficient representation of the voxel profiles using few basis functions. The coefficients in $\boldsymbol{U}$, along with the singular values, are shown in a. The singular values of the data ($\boldsymbol{\Gamma}$) decay rapidly to 0, indicating that the data can be represented efficiently using few basis functions. The pseudo-periodicity of the data is exploited by the l_1 Fourier sparsity regularization scheme, using the sparse representation of the intensity profiles in the temporal Fourier transform (x-f space) as seen in b. Panel c shows the sparse coefficients obtained from the BCS scheme. Similar to the nuclear norm minimization scheme, BCS learns the dictionary of the basis functions from the data itself, thus adapting to the dynamic content of the time series. The adaptation of the dictionary to the signal provides sparser representations, which in turn translates to improved reconstructions. Figure 1 can be viewed online in color at www.investigativeradiology.com.

dimension (x-f space) (see Fig. 1b). The convex optimization problem is formulated as follows:

$$\boldsymbol{\Gamma}^* = \arg\min_{\boldsymbol{\Gamma}} \underbrace{\| \mathcal{A}(\boldsymbol{\Gamma}) - b \|_F^2}_{\text{data consistency term}} + \underbrace{\lambda \| \mathscr{F}_t(\boldsymbol{\Gamma}) \|_{l_1}}_{\text{temporal Fourier sparsity}}, \quad (4)$$

where $\mathscr{F}_t$ is the Fourier transform in the temporal direction. The l_1 norm in the second term enforces sparsity on the Fourier coefficients along the temporal dimension. This approach is a widely used scheme and has similarities to the k-t SPARSE[25,26] and k-t FOCUSS[27,28] schemes, whereas the specific algorithms used to solve them are different from our implementation. The recovery implicitly assumes that the intensity profiles of the voxels are sparse linear combinations of Fourier exponentials.

- BCS[22,29] : The temporal profile for each pixel is modeled as a sparse linear combination of atoms from a learned dictionary. Because the dictionary that is learned from the undersampled measurements is subject specific, not necessarily orthogonal and may be overcomplete, it provides a richer representation of the data. The sparsity enforced on the dictionary coefficients suggests that very few temporal basis functions are sufficient to model the temporal profiles at any pixel. This results in lower degrees of freedom and hence minimizes artifacts at high acceleration factors. The data $\boldsymbol{\Gamma}$ are modeled as a product of the sparse coefficient matrix $\mathbf{U}$ and dictionary $\mathbf{V}$. The signal recovery from the undersampled measurements is posed as a constrained optimization algorithm as shown below:

$$[\mathbf{U}^*, \mathbf{V}^*] = \arg\min_{\mathbf{U},\mathbf{V}} \underbrace{\| \mathcal{A}(\mathbf{UV}) - b \|_F^2}_{\text{data consistency term}} + \underbrace{\lambda \| \mathbf{U} \|_{1_1}}_{\text{Sparsity on spatial weights}} \quad \textit{such that } \| \mathbf{V} \|_F^2 < 1 \quad (5)$$

The second term is the sparsity promoting l_1 norm on the coefficient matrix $\mathbf{U}$. The optimization problem is constrained by imposing unit Frobenius norm on the overcomplete dictionary $\mathbf{V}$, which makes the recovery problem well posed and avoids scale ambiguity issues. Our experiments[22] show that the joint estimation of the basis functions and its coefficients from a golden angle radial trajectory is well posed, thanks to the oversampling of center of k-space offered by radial trajectories.

- View-sharing: In this scheme, each frame of the data set is reconstructed by combining information from a few adjacent frames. For this study, we combined 200 radial spokes to reconstruct each frame with a step size of 16 to match the temporal resolution with other reconstruction schemes.

Implementation of Constrained Algorithms

All the above constrained algorithms are implemented using alternating minimization algorithms; these schemes alternate between

(a) a backward mapping from k-space to image space to enforce data consistency and (b) a projection step, which is a shrinkage or projection operator. These algorithms are guaranteed to converge to the global minimum of the cost function, provided it is convex (nuclear norm and Fourier sparsity regularization, specified by equations (3) and (4) respectively). Because of the nonlinear nature of the above algorithms, coupled with a nonuniform k-space sampling, it is complex to analyze the spatial and temporal smoothing behavior of the algorithms. However, the projection step provides useful insights on how each of these schemes removes the aliasing patterns that results from the undersampling. We perform a brief analysis of the constrained algorithms to obtain more insights of the tradeoffs involved in accelerating using these schemes in Appendix A.

The discussion in Appendix A shows, constrained schemes that model the temporal profiles reduce aliasing artifacts by nonlocal view-sharing. Specifically, they recover each pixel in the data set as a weighted linear combination of other pixels in the data set, possibly distant from it in time. Note that this approach is drastically different from classical view-sharing schemes that combine the data from nearby frames to recover each frame; we term such classical view-sharing schemes as local to differentiate them from the nonlocal ones discussed above. Nonlocal averaging combines information from images in similar respiratory phases that are distant in time, thus minimizing the temporal blurring introduced by local view-sharing schemes, while achieving good suppression of noise-like aliasing artifacts. The analysis shows that the BCS and l_1 Fourier sparsity regularization schemes perform spatially varying nonlocal view-sharing, whereas the nuclear norm minimization scheme performs space invariant nonlocal view-sharing. The adaptation of the view-sharing strategy with the spatial location enables BCS and l_1 Fourier sparsity regularization to achieve improved denoising performance.

Experiment Details

The fully sampled data set (acquired with 256 radial spokes) was retrospectively undersampled using 16 radial spokes per frame, corresponding to an acceleration factor of 8. This retrospectively undersampled data set was reconstructed with the above-mentioned nuclear norm minimization scheme, the l_1 Fourier sparsity regularization scheme, BCS, and the standard view-sharing scheme. The reconstructed data were compared with the fully sampled acquisition. To study the performance of the BCS scheme as a function of acceleration, the 2D data set undersampled using 20, 16, 12, and 10 radial spokes corresponding to acceleration factors of 6.4, 8, 10.2, and 12.8, respectively. The slice-by-slice reconstruction was performed for all the 3D-DMRI data sets using the above-mentioned schemes. All the reconstructions were performed in MATLAB on a desktop computer (Intel Xeon E5-1620 with 8 core CPUs, 3.6 GHz processor, and 32 GB RAM) with a 5.6 GB NVDIA graphical processing unit.

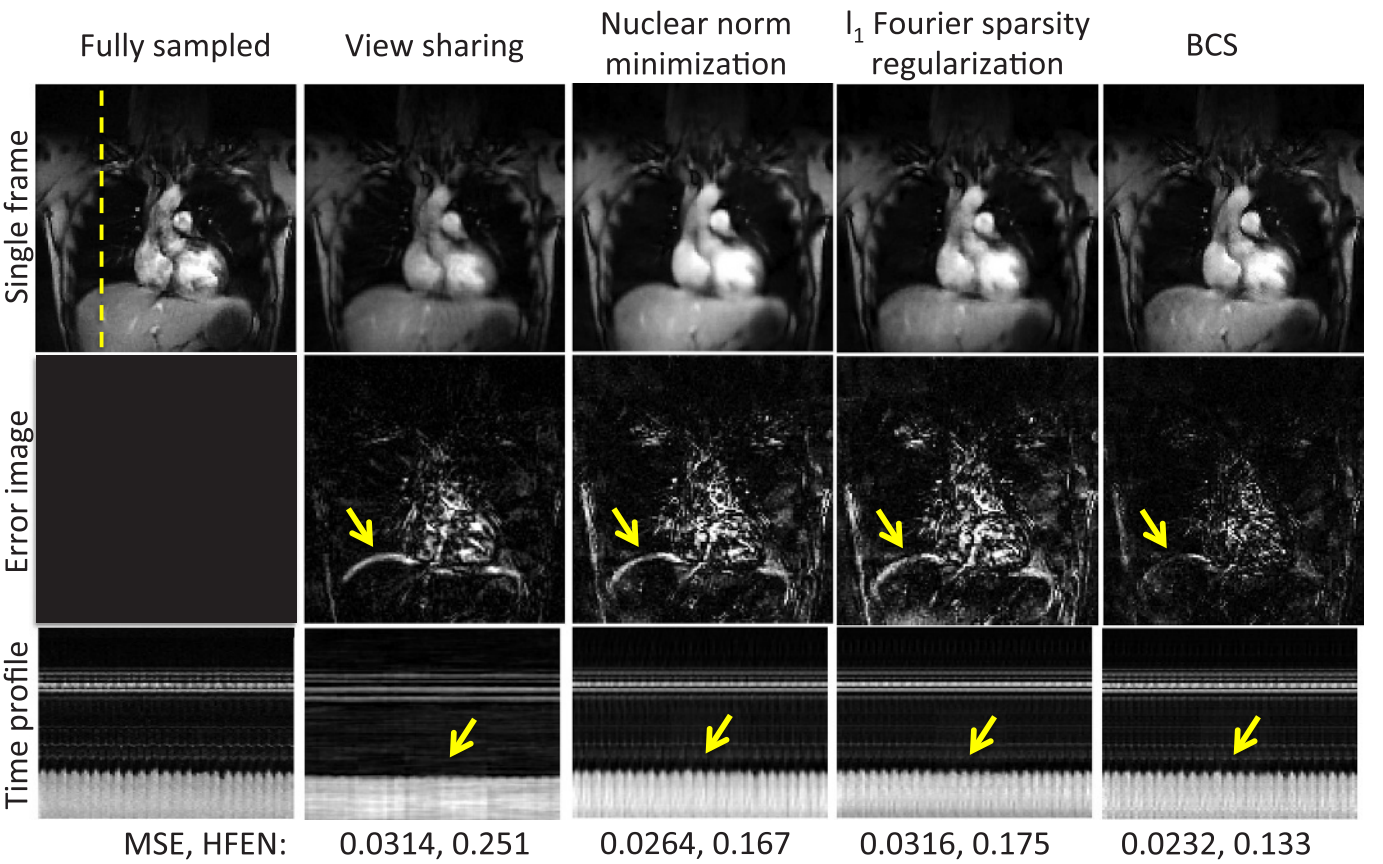

FIGURE 2. Comparison of different schemes on 2D fully sampled data set: The figure shows comparison of reconstructions obtained from view-sharing, the nuclear norm minimization scheme, the l_1 Fourier sparsity regularization scheme, and the BCS scheme with the fully sampled data. The top row shows a single frame for each of the schemes. The middle row shows the error images with respect to the fully sampled data, and the last row shows the time profiles of all the schemes at a cross-section shown by the yellow dotted line. From the MSEs and the HFEN metric, we observed that BCS gives superior performance than other schemes do. All the schemes except BCS suffer from spatiotemporal blurring, as shown by the yellow arrows in the error images and time profiles. Figure 2 can be viewed online in color at www.investigativeradiology.com.

Image Quality Analysis

To compare reconstructions, we used the following metrics:

- Mean square error (MSE): In the 2D experiments, the fully sampled ground truth data were used as reference to calculate the reconstruction errors. The optimal regularization parameter λ was chosen such that the error between reconstructions and the fully sampled data, specified by

$$\mathrm{MSE} = \left(\frac{\|\mathbf{\Gamma}_{\mathrm{recon}} - \mathbf{\Gamma}_{\mathrm{orig}}\|_F^2}{\|\mathbf{\Gamma}_{\mathrm{orig}}\|_F^2} \right), \quad (6)$$

  was minimized. However, the MSE metric could not be used for the 3D experiments, as the fully sampled ground truth was not available. Hence, to optimize for λ, we used the L-curve strategy.[30]
- Normalized high-frequency error metric (HFEN): The HFEN metric[31] gives a measure of spatial blurring of the image and the quality of fine features and edges. The HFEN metric is defined as

$$\mathrm{HFEN} = \frac{1}{N} \sum_{i=1}^{N} \left(\frac{\|\mathrm{LoG}(\mathbf{\Gamma}_{\mathrm{ref},i}) - \mathrm{LoG}(\mathbf{\Gamma}_{\mathrm{recon},i})\|_2^2}{\|\mathrm{LoG}(\mathbf{\Gamma}_{\mathrm{ref},i})\|_2^2} \right), \quad (7)$$

  where N is the number of pixels in the image and LoG is the Laplacian of the Gaussian filter that captures edges. The filter specifications are kernel size of 15×15 pixels, with a standard deviation of 1.5 pixels.[31] The regularization parameters for all the schemes were optimized using the HFEN and MSE values in case of 2D experiments.
- Qualitative evaluation-clinical scoring: Each of the 3D dynamic reconstructions was evaluated for spatial resolution, temporal resolution, and artifacts by 2 expert cardiothoracic radiologists using a 4-point scale (4: outstanding diagnostic quality; 3: good diagnostic quality; 2: average diagnostic quality; 1: limited diagnostic quality; and 0: uninterpretable). The image data sets were viewed using OsiriX.

Image Postprocessing to Demonstrate the Utility of 3D-DMRI

To demonstrate the potential applications of this work, the lung was segmented using a region-growing algorithm implemented in MATLAB after reconstructing the 3D dynamic data using the BCS scheme, the nuclear norm minimization scheme, and the l_1 Fourier sparsity regularization scheme. This analysis was done for the data set collected with the tidal breathing maneuver on subject 8. The analysis was repeated for the same subject with deep breathing maneuver using the

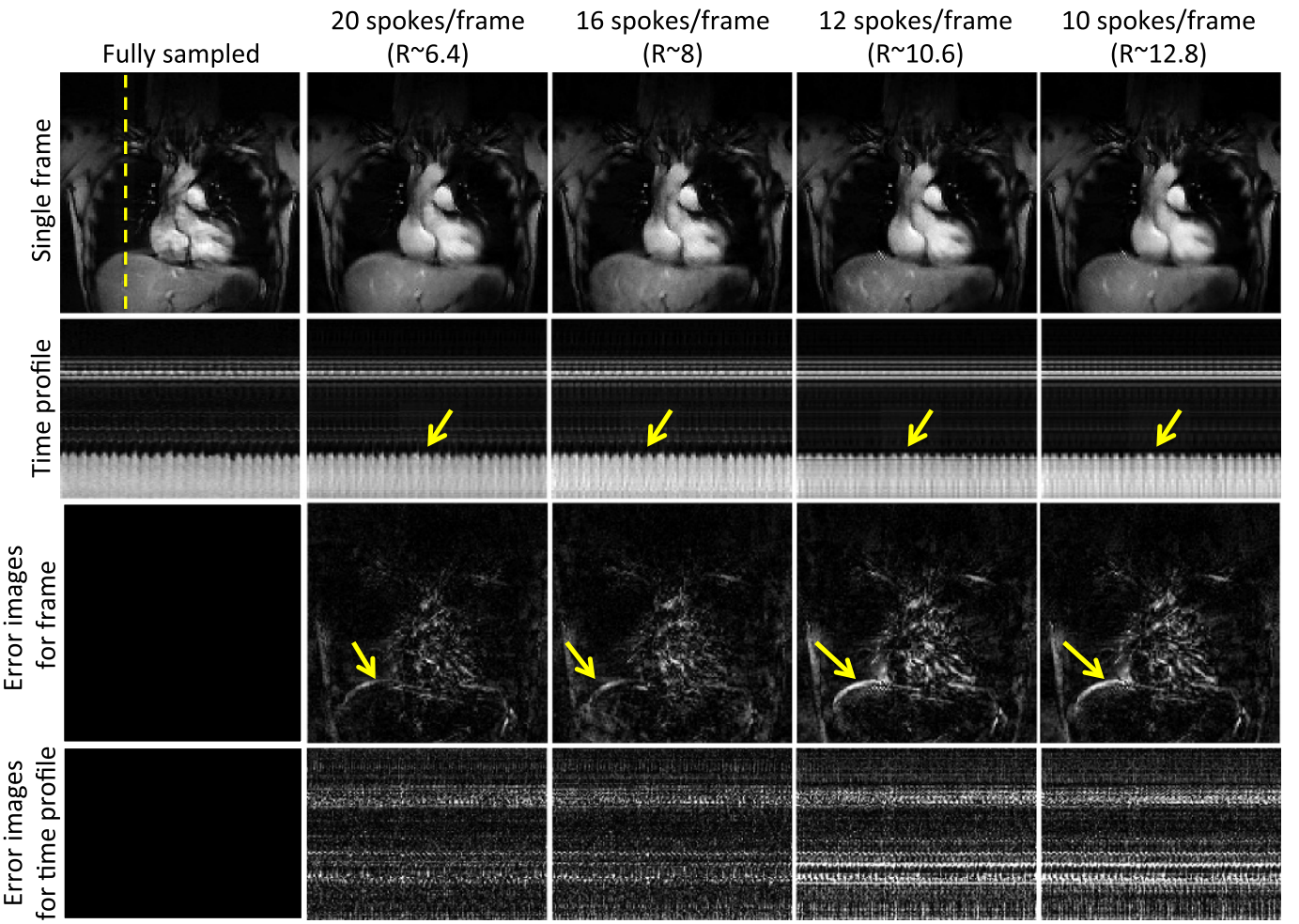

FIGURE 3. Performance of the BCS scheme at different acceleration factors: The figure shows the single frame (row 1), the time profiles (row 2), and the corresponding error images (rows 3–4) of reconstructions obtained by retrospectively undersampling the data set with 20, 16, 12, and 10 radial spokes per frames, resulting in acceleration factors (R) of 6.4, 8, 10.2, and 12.8, respectively. Reliable reconstructions are achieved up to R = 8. Beyond R = 8, we began to observe temporal blurring, as shown by the arrows in the error images. All the images are in the same scale. Figure 3 can be viewed online in color at www.investigativeradiology.com.

BCS reconstructed data. The lung volume was calculated in terms of the number of pixels within the lung region. The velocity maps of the diaphragm were obtained using optical flow method,[32] which was implemented using a multiscale approach.

RESULTS

Dynamic 2D Experiments

The performance of all the schemes was first evaluated by retrospectively undersampling a 2D fully sampled data set. Figure 2 shows a spatial frame from the dynamic 2D data set (top row), the corresponding error images (middle row), and the time profile at a cross-section shown by the yellow line in spatial frame (last row). The columns correspond to the fully sampled data set (first column) and the different reconstructions from retrospectively undersampled data. All the comparisons were done at an undersampling factor of 8 (using 16 radial spokes per frame). We observed that the reconstructions from the nuclear norm minimization and l_1 Fourier sparsity regularization schemes suffer from spatiotemporal blurring, especially along the diaphragm borders, as indicated by the arrows in the error images. The local view-sharing scheme combines information from adjacent frames (13 adjacent frames were combined for reconstruction of each frame), which results in significant blurring of the respiratory motion as seen from the time profiles. The BCS scheme has the lowest MSE errors (0.0232) and HFEN values (0.133), which indicates superior reconstruction and less spatiotemporal blurring as compared with the other schemes.

Figure 3 shows the comparisons of the reconstructions from 20, 16, 12, and 10 radial spokes per frame with the fully sampled data. We observed that BCS gives reliable reconstructions with 20 and 16 radial spokes per frame. A reconstruction from 12 or 10 radial spokes results in temporal blurring, as shown by the arrows. In the 3D experiments, we fixed the number of radial spokes per frame to 16 for all the schemes.

Dynamic 3D Experiments

Figure 4 shows the comparisons of the 4 schemes for a subject. The figures show a single frame and a time profile along the cross-section for 4 of the 16 slices. We observed that the local view-sharing scheme suffers from temporal blurring and aliasing artifacts. The nuclear norm minimization scheme provides better reconstructions than view-sharing does, but it exhibits more spatiotemporal blurring than the BCS reconstructions, as shown by the arrows. Reconstructions from both the l_1 Fourier sparsity regularization scheme and the BCS scheme show comparable image quality in the spatial domain, as seen from the spatial frames in both figures. However, the l_1 Fourier sparsity regularization scheme results in higher temporal blurring than BCS does. In slices where the tissue motion is very subtle (slice 6 in Fig. 4), BCS preserves the motion, whereas all other schemes result in blurring of temporal details. One of the radiologists carefully analyzed the performance of all the schemes as a function of slice position while clinical scoring

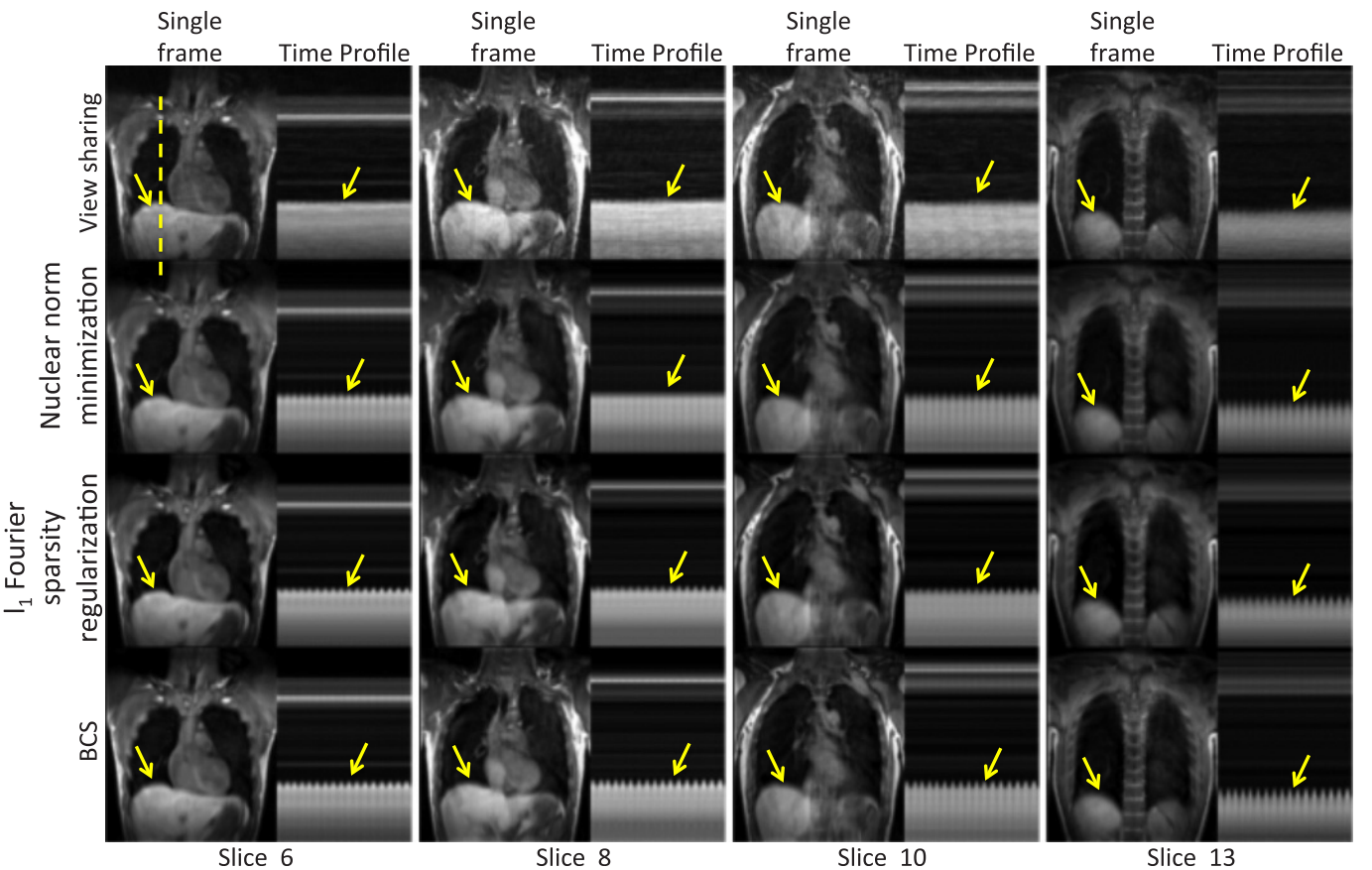

FIGURE 4. Comparison of different schemes on dynamic 3D free breathing: The figure shows comparison between view-sharing, the nuclear norm minimization scheme, the l_1 Fourier sparsity regularization scheme, and the BCS scheme (rows 1–4) for 4 of the 16 slices on subject 2. We observed that the BCS gives better reconstructions than other schemes do. It is seen that BCS shows superior spatiotemporal fidelity in comparison with the other schemes (see yellow arrows). Figure 4 can be viewed online in color at www.investigativeradiology.com.

as shown in Figure 5 and found that the performance of the BCS scheme was relatively insensitive to the slice position compared with other schemes. Specifically, the reconstructions of the anterior and posterior slices of the lung (second and third columns of Fig. 5), obtained by the other schemes, showed higher degradation in image quality than the more central slices (first column of Fig. 5), especially in terms of spatial and temporal blurring (pointed by arrows).

Table 1 shows the visual scores of all the 4 schemes by both the radiologists (denoted as R1 and R2) based on 3 different factors: (*a*) aliasing artifacts, (*b*), temporal blurring, and (*c*) spatial blurring. The scores from both the radiologists suggest that the BCS scheme performs better than other schemes in the temporal blurring (Table 1, part b) and spatial blurring (Table 1, part c) categories. The improved performance of BCS can be attributed to the spatially varying nonlocal averaging feature and its ability to adapt to the cardiac and respiratory patterns of the specific subject. The qualitative scores for aliasing artifacts are roughly the same for the nuclear norm minimization scheme (3.75 ± 0.7, 2.62 ± 1.19) and the BCS scheme (and 3.62 ± 0.51, 2.62 ± 0.91); the 2 figures within parentheses denote the mean scores from R1 and R2, respectively, and the number following ± is the standard deviation. We observed that the interobserver variability is high for this category compared with the others. The scores for the view-sharing scheme are much lower than those for the other 3 schemes for all the 3 categories from both radiologists. In summary, the BCS scheme, the nuclear norm minimization scheme, and the l_1 Fourier sparsity regularization scheme perform comparably in terms of minimizing the aliasing artifacts. However, BCS scheme outperforms all other schemes in terms of minimizing spatiotemporal blurring.

Figure 6 shows the lung volume as a function of time and the lung segmentation contours for the BCS, nuclear norm minimization,

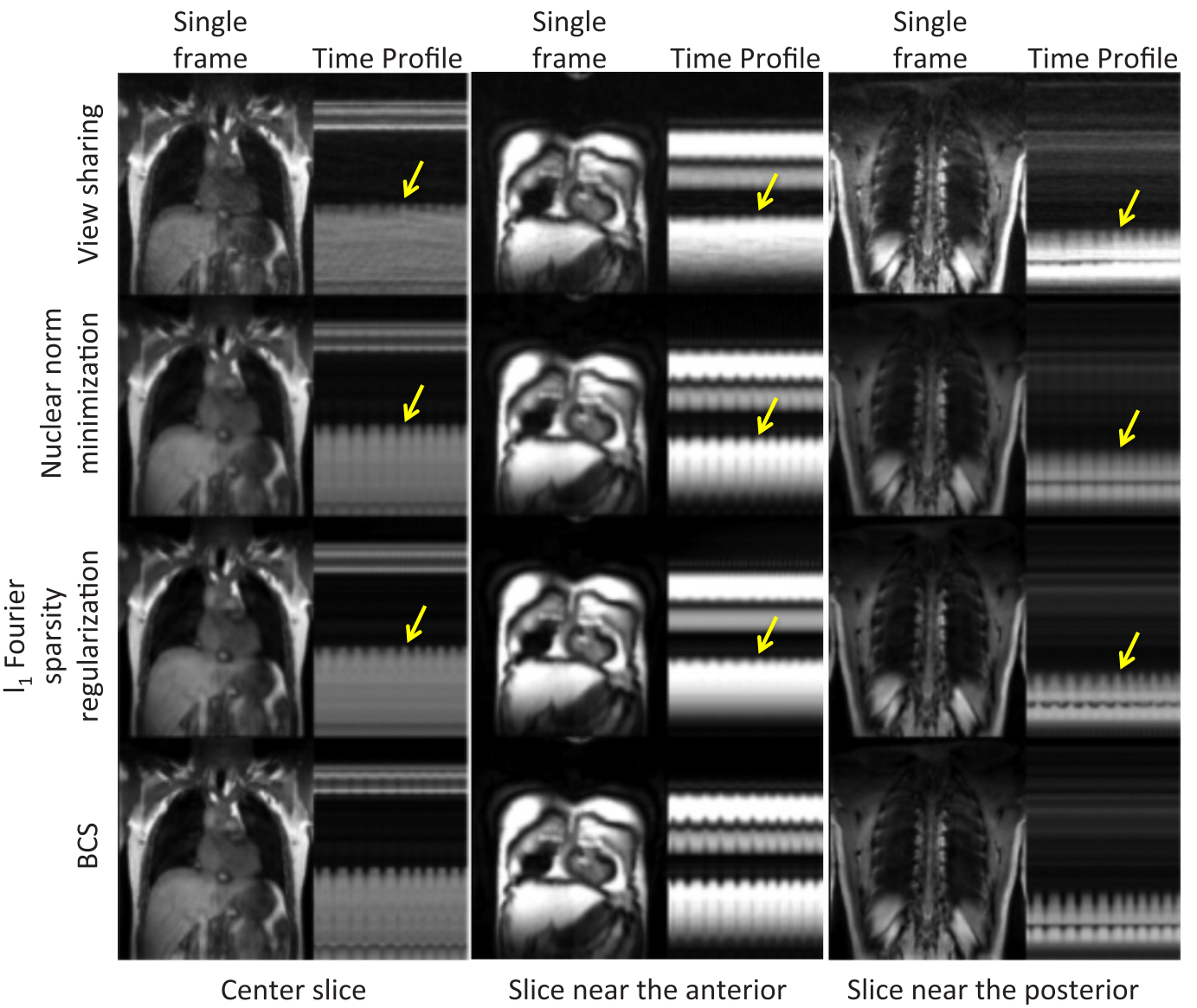

FIGURE 5. Performance of all the schemes as a function of slice position: The figure shows comparison between view-sharing, the nuclear norm minimization scheme, the l_1 Fourier sparsity regularization scheme, and the BCS scheme (rows 1–4) for slices positioned at the center (first column), anterior (second column), and posterior (third column) of the lung. We observed that all schemes except the BCS scheme suffer from higher temporal blurring in the slices at anterior and posterior regions of the lung than those in the center region. The BCS scheme is relatively insensitive to the slice position as compared with other schemes. Figure 5 can be viewed online in color at www.investigativeradiology.com.

TABLE 1. Clinical Scores of 8 3D-DMRI Data Sets for All 4 Schemes by Both Radiologists

	BCS		Nuclear Norm Minimization		l_1 Fourier Sparsity Regularization		View-Sharing	
	R1	R2	R1	R2	R1	R2	R1	R2
a. Clinical scores: aliasing artifacts								
Subject 1	4	1	4	1	3	1	1	1
Subject 2	3	3	4	3	2	3	1	1
Subject 3	4	4	4	4	4	4	1	2
Subject 4	4	3	2	3	3	3	1	2
Subject 5	4	3	4	3	2	3	1	2
Subject 6	4	2	4	2	4	2	1	1
Subject 7	3	3	4	4	3	2	1	1
Subject 8	3	2	4	1	3	1	1	0
Average scores	3.62 ± 0.51	2.62 ± 0.91	3.75 ± 0.7	2.62 ± 1.19	3 ± 0.76	2.37 ± 1.06	1 ± 0	1.25 ± 0.7
b. Clinical scores: temporal blurring								
Subject 1	4	4	2	3	3	3	0	0
Subject 2	4	4	3	3	3	4	2	1
Subject 3	4	4	1	3	2	3	1	1
Subject 4	4	4	2	3	3	3	1	1
Subject 5	4	4	3	4	2	4	0	1
Subject 6	4	4	2	2	2	2	1	1
Subject 7	4	4	1	2	2	2	0	1
Subject 8	4	4	3	3	2	3	0	0
Average scores	4 ± 0	3.87 ± 0.35	2.21 ± 0.83	3 ± 0.75	2.37 ± 0.51	2.5 ± 1.3	0.62 ± 0.74	0.75 ± 0.46
c. Clinical scores: spatial blurring								
Subject 1	4	4	2	3	3	3	1	4
Subject 2	3	4	2	4	3	2	1	3
Subject 3	4	4	2	4	3	3	1	4
Subject 4	4	4	2	4	3	3	1	4
Subject 5	4	4	3	4	3	2	1	4
Subject 6	4	4	3	4	3	2	1	4
Subject 7	4	4	2	4	3	3	1	3
Subject 8	4	4	2	4	3	3	1	3
Average scores	3.87 ± 0.35	4 ± 0	2.25 ± 0.46	3.87 ± 0.35	3 ± 0	2.63 ± 0.52	1 ± 0	3.62 ± 0.51

We observes that all schemes except view-sharing are comparable in terms of minimizing aliasing artifacts for each radiologist, as seen in part a. However, there is interobserver disagreement (different scores by R1 and R2) in the scores. The BCS scheme has higher scores than all the other schemes in temporal and spatial blurring categories (parts b and c), which indicates that the BCS has minimal spatiotemporal blurring as compared with the other schemes. There is good agreement between the scores by both radiologists for temporal and spatial blurring categories.

and l_1 Fourier sparsity regularization schemes on 1 subject with tidal breathing maneuver. The change in lung volume for BCS (approximately 200 mL) was significantly different from that for the nuclear norm minimization scheme (around 150 mL) and l_1 Fourier sparsity regularization scheme (<100 mL). The contours depict the boundary of the lung obtained from the segmentation of the reconstructions. The 2 time points (a and b) in the figure correspond to maximum inspiratory volume. From the contours, we observed that at maximum inspiration, the boundary of the lung for the nuclear norm minimization and l_1 Fourier sparsity regularization schemes is higher than that for the BCS scheme, which means that the volume of the lung is less than that for the BCS scheme. This is attributed to higher temporal blurring in the other 2 schemes as compared with the BCS scheme. Time point c corresponds to maximum expiration. From the last row in the figure, we observed that the segmentations from all the 3 schemes are the same. The tidal volume analysis could not be performed on the view-sharing scheme because the reconstructions in this case suffered from aliasing artifacts, which resulted in poor segmentation of the lungs.

Figure 7 shows the change in volume as a function of time and the segmented lung volumes for 1 subject with tidal breathing and deep breathing maneuvers. The lung was segmented from the reconstructions obtained using the BCS scheme. The change in lung volume was approximately 200 mL. The normal minute ventilation was calculated as tidal volume × number of breathing cycles in a minute, which was found to be 4 L/min. In case of deep breathing maneuver, we measured the supine inspiratory capacity, which was found to be 1.5 L. This correlates well with the literature for normal subjects in the supine position.

The motion of the diaphragm as tracked using an optical flow method is shown in Figure 8. Two sets of 2 frames each, 1 set with a large change in the diaphragm position (red segment and blue segment) and 1 with little change in the diaphragm position (green segment and orange segment), were chosen during inspiration and expiration. The velocity vector maps and the color-coded velocity maps are shown in each of the cases. Figures 8a and b show the velocity maps during inspiration and Figures 8c and d show the velocity maps during expiration. From the color-coded velocity maps, we observed that a higher displacement in the diaphragm position (higher diaphragm velocity)

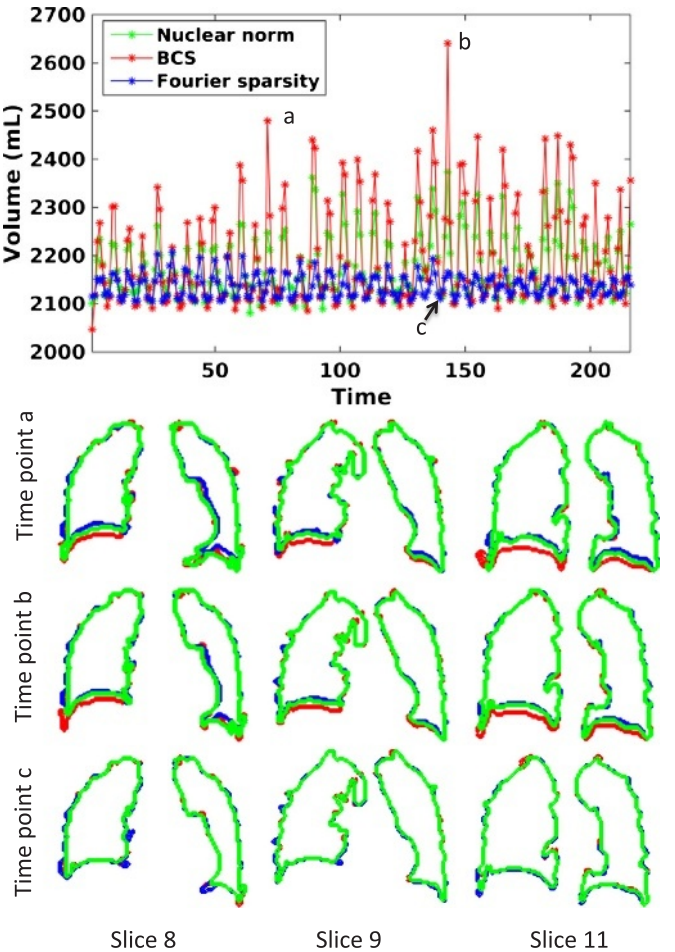

FIGURE 6. Comparison of BCS, Nuclear norm minimization, and l_1 Fourier sparsity regularization schemes for changes in lung volume as a function of time for subject 8: The plot shows the volume of lung (in milliliters) as a function of time obtained from reconstructions using BCS (in red), nuclear norm minimization (in green), and l_1 Fourier sparsity regularization (in blue). The second, third, and fourth rows show the lung segmentation contours for the 3 schemes at 3 time points a, b, and c, respectively. The contours are shown for 3 of the 18 slices. From the plot as well as from the segmentations, we can see that the nuclear norm minimization and l_1 Fourier sparsity regularization schemes suffer from considerable temporal blurring. Note that the segmentations at time point c (peak expiration) are almost the same. This is expected because the position of the diaphragm changes more during inspiration than during expiration. Figure 6 can be viewed online in color at www.investigativeradiology.com.

correlates well with the observed change in lung volume between the corresponding frames during both inspiration and expiration.

DISCUSSION

The application of compressed sensing, together with parallel imaging to accelerate 3D dynamic imaging of lung volumes and diaphragm motion, has not been studied extensively in the past. We evaluated the performance of 4 different schemes (view-sharing, nuclear norm minimization scheme, l_1 Fourier sparsity regularization scheme, and BCS scheme) in accelerating 2D and 3D dynamic free breathing MRI of the thorax in 8 normal subjects. In both our 2D and 3D experiments, we observed that the BCS scheme yields superior reconstructions compared with other schemes qualitatively and quantitatively. The BCS scheme, along with golden angle sampling patterns, offered a temporal resolution of ~500 milliseconds and a spatial resolution of $2.7 \times 2.7 \times 10$ mm^3 with whole lung coverage, while maintaining image quality. To the best of our knowledge, this is the first work that demonstrates temporal resolution of less than 1 second, along with whole coverage of the thorax, which enables 3D free breathing dynamic imaging of lung volumes and diaphragm motion.

We observed that the classical view-sharing scheme suffers from severe temporal blurring as it combines information from adjacent frames. Because the data acquired are free breathing, the respiratory motion between adjacent frames is very high. Hence, the view-sharing approach results in extensive blurring. In contrast, the constrained schemes can be thought of as nonlocal view-sharing schemes; their ability to combine information from frames/pixels that are highly similar enables them to reduce blurring. We observed that the ability of the BCS and the l_1 Fourier sparsity regularization scheme to spatially adapt the nonlocal averaging depending on the dynamics enables them to provide better reconstructions than the nuclear norm minimization scheme. In dynamic data sets with regions corresponding to strikingly different dynamics (eg, cardiac and respiratory motion), the ability to spatially adapt the nonlocal averaging can give improved results. The l_1 Fourier sparsity regularization scheme is sensitive to irregular voxel profiles resulting from nonlinear interactions between cardiac and respiratory motion. This is because irregular voxel profiles result in a higher number of nonzero Fourier coefficients, thus disrupting the sparsity assumption. The regularity of the breathing patterns will vary from subject to subject, leading to inconsistent performance of the l_1 Fourier sparsity regularization scheme. These schemes may not be reliable in the dynamic assessment of lung volumes

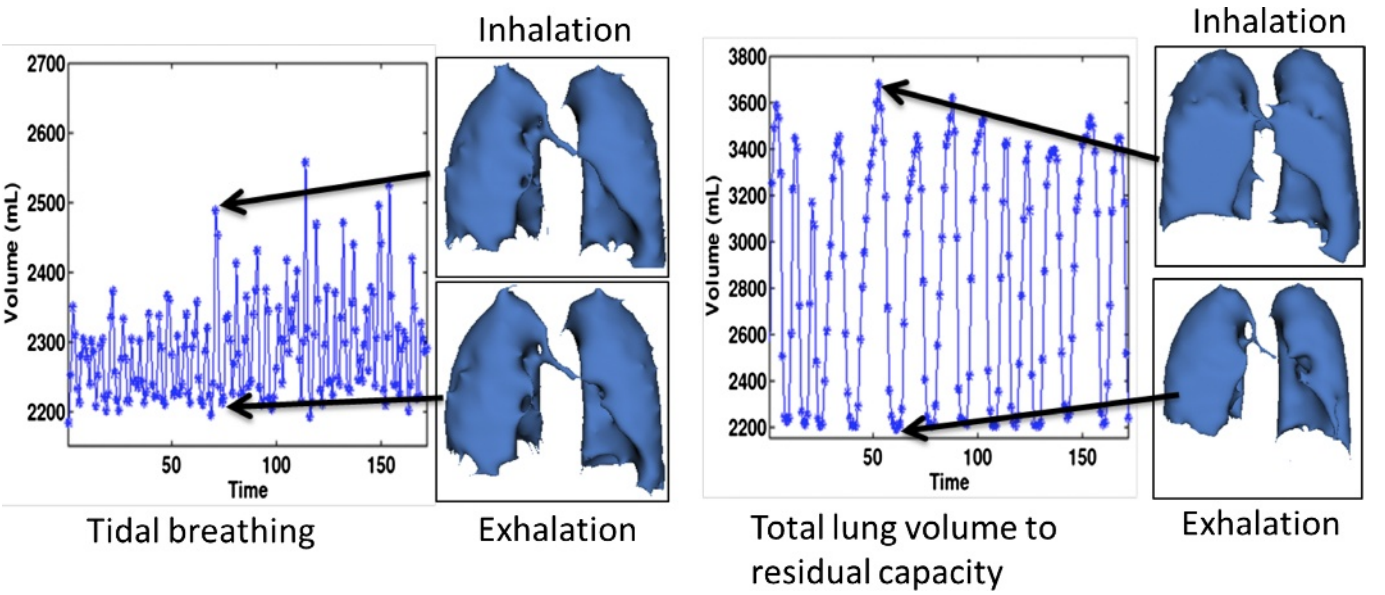

FIGURE 7. Changes in lung volume as a function of time: The figure shows the changes in lung volumes as a function of time in case of tidal breathing maneuver (shown on the left) and deep breathing maneuver from total lung capacity to functional residual capacity (shown on the right). The segmented lung volumes during peak inhalation and peak exhalation are also shown for both breathing maneuvers. The tidal volume was measured to be approximately 200 mL and the normal minute ventilation was around 4 L/min. The supine inspiratory capacity was measured to be 1.5 L. Note that these numbers are for the supine position. Figure 7 can be viewed online in color at www.investigativeradiology.com.

during free breathing in patients with emphysema or other causes of dyspnea. The patient-specific dictionaries in the BCS scheme may be a better choice in patients who are short of breath; these learned basis functions will result in a sparser data representation and hence provide reliable recovery from fewer measurements. In addition, incoherent sampling by golden angle ordering aids in obtaining a sparser representation, leading to superior reconstructions. Other interleaved sampling patterns may also lead to similar accelerations; however, a thorough validation of this claim is beyond the scope of this article. We observed that there are currently several different flavors of compressed sensing implementations, which may be applied to this specific problem. We restrict our comparisons in this work to few of the state-of-the-art dynamic imaging schemes because rigorous comparison with all of them is beyond the scope; alternate implementations of these algorithms may produce higher quality reconstructions with less temporal/spatial blurring and aliasing artifacts than reported in this work. We have used the radial FLASH sequence to demonstrate the feasibility of the BCS scheme. However, this scheme can be combined with more efficient trajectories with longer readouts (e.g. multishot echo-planar imaging, multishot spiral) to further improve spatial and temporal resolution and TE, which is the focus of our current work. The acceleration provided by BCS can enable us to keep the readout duration small enough to minimize B0-induced distortions and losses.

The average scores from both the radiologists indicate good agreement for spatial and temporal blurring criteria. There is relatively higher interobserver variability in scores for the aliasing artifact criterion, but the mean scores from both the radiologists suggest that the BCS scheme performs better. The postscoring discussion revealed that 1 of the radiologists gave more importance to the blurring and artifacts that affected the diaphragm motion or diaphragm delineation. In contrast, the other radiologist rated the data sets based on the blurring and artifacts in the whole image rather than placing more emphasis on the diaphragm. This explains the bias in the scores pertaining to spatial blurring. The number of subjects is insufficient to perform statistical analysis for interobserver agreement.

Our preliminary results using the BCS scheme for dynamic imaging of lung volumes and diaphragm motion obtained from a single data set seem promising. The normal minute ventilation in a resting adult in the upright position is about 5 to 8 L/min.[33,34] However, the normal minute ventilation in the supine position is less than in the upright position,[33,34] and all of our MRI images were obtained in the supine position. The measured minute ventilation of 4 L/min is within the normal range for a supine subject. The measurement of minute ventilation is useful in a number of disease mechanisms that produce arterial hypercapnia.[35] The lung volumes were segmented using a simple region growing approach with minimal user interference. There are more sophisticated lung segmentation algorithms, including the fuzzy-connectedness algorithm, that could be performed to further improve our lung segmentation.

The proposed imaging protocol acquires 3D data with 16 partitions using the stack of stars trajectory; the sampling pattern is the same for all the partitions, which enables slice-by-slice recovery. Although the number of slices is sufficient for good depiction of diaphragm and lung volume dynamics in normal subjects, it may not be sufficient for obese subjects. Improved slice coverage may be obtained using fully 3D recovery exploiting the spatial redundancies and using 3D trajectories. The current sequence uses a 3D stack of stars trajectory, where the sampling along the k_z direction is uniform. Because the k_z direction is fully sampled (except in some cases where partial Fourier recovery is used), we compute a Fourier transform along k_z and recover each slice independently. We anticipate that using different angles for different k_z planes as well as sampling different k_z planes with different sampling densities will provide a more incoherent and appropriate sampling pattern. This strategy may result in improved recovery, but at the cost of higher computational complexity and memory demand, because we cannot decouple the problem to solve for each slice independently. The golden angle-sampling pattern was used to achieve incoherent sampling across timeframes; however, other interleaved patterns can be used with BCS to provide these accelerations. Our future work will focus on these and other image reconstruction schemes that are optimized for individual patients with respiratory disorders, including chronic obstructive pulmonary disease, asthma, and cystic fibrosis.

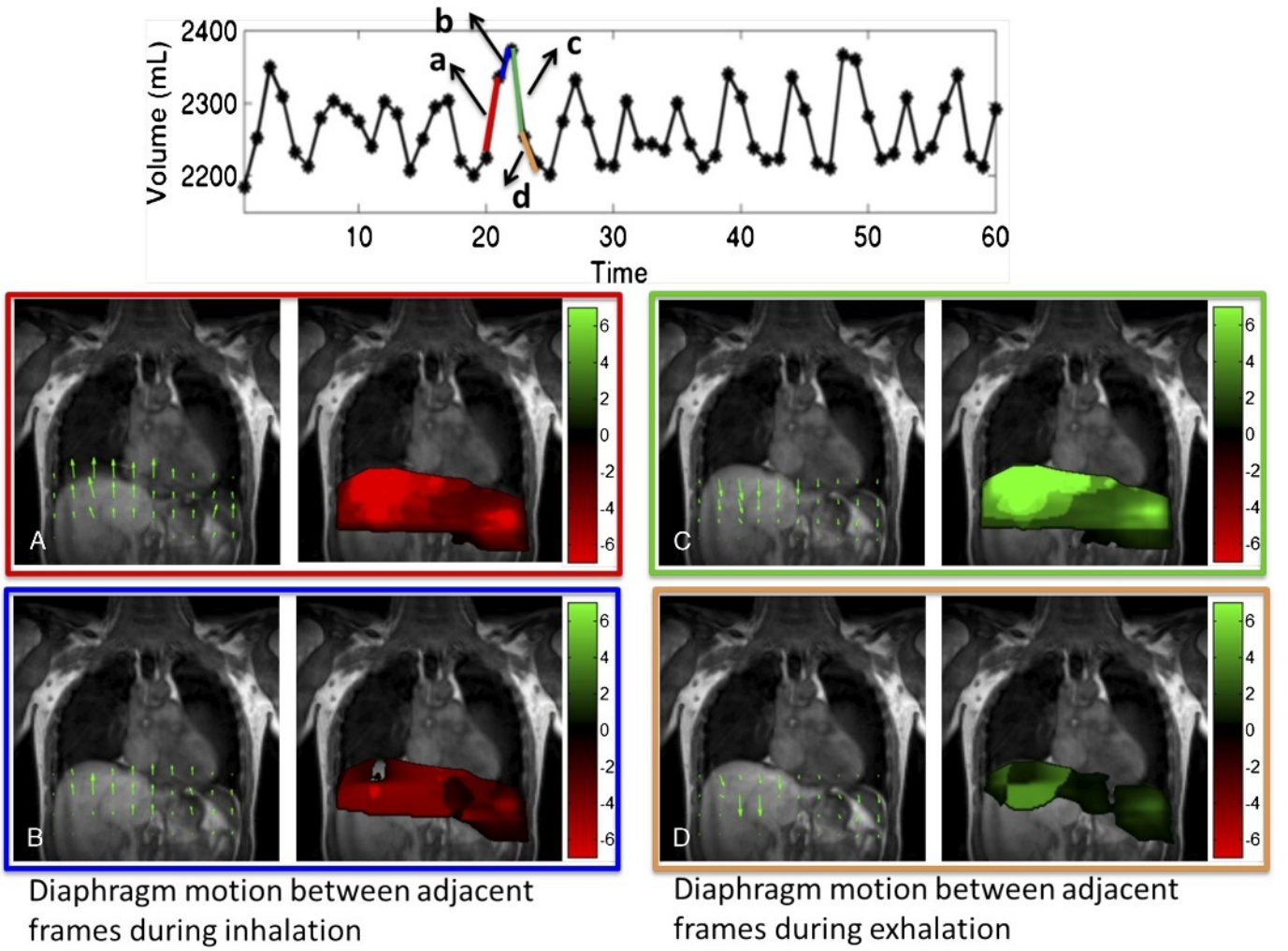

FIGURE 8. Tracking diaphragm motion using velocity maps: The motion of the diaphragm was tracked at 2 time points between inspiration (a, b) and 2 time points between expiration (c, d). The velocity from inspiration to expiration is considered positive (in green) and the velocity from expiration to inspiration is considered negative (in red). The velocity field maps and the color-coded velocity maps are shown for all 4 cases. The change in lung volume shown by blue segment is much lesser than the change in lung volume shown by red segment. This translates to higher diaphragm motion in frames in red segment as compared with the blue segment as seen from the color coded velocity maps in a and b. Similar results were observed during both inspiration and expiration. Figure 8 can be viewed online in color at www.investigativeradiology.com.

In conclusion, our study indicates that the BCS scheme gives individualized reconstructions with diagnostically useful image quality and minimal spatiotemporal blurring as compared with other accelerated imaging schemes. We showed that 3D dynamic imaging of lung volumes and diaphragm motion with high spatial and temporal resolution is achievable using the BCS scheme.

ACKNOWLEDGMENTS

The authors thank the reviewers for their valuable suggestions and comments.

REFERENCES

1. Gierada DS, Curtin JJ, Erickson SJ, et al. Diaphragmatic motion: fast gradient-recalled-echo MR imaging in healthy subjects. *Radiology*. 1995;194:879–884.
2. Craighero S, Promayon E, Baconnier P, et al. Dynamic echo-planar MR imaging of the diaphragm for a 3D dynamic analysis. *Eur Radiol*. 2005;15:742–748.
3. Polkey MI, Kyroussis D, Hamnegard C-H, et al. Diaphragm strength in chronic obstructive pulmonary disease. *Am J Respir Crit Care Med*. 1996; 154:1310–1317.
4. Gold W, Boushey H. Pulmonary function testing. *Textbook of Respiratory Medicine*. Philadelphia, PA: WB Saunders Company; 2000;vol 1:844–846.
5. Gauthier AP, Verbanck S, Estenne M, et al. Three-dimensional reconstruction of the in vivo human diaphragm shape at different lung volumes. *J Appl Physiol*. 1994;76:495–506.
6. Kondo T, Kobayashi I, Taguchi Y, et al. A dynamic analysis of chest wall motions with MRI in healthy young subjects. *Respirology*. 2000;5:19–25.
7. Cluzel P, Similowski T, Chartrand-Lefebvre C, et al. Diaphragm and chest wall: assessment of the inspiratory pump with MR imaging-preliminary observations. *Radiology*. 2000;215:574–583.
8. Kiryu S, Loring SH, Mori Y, et al. Quantitative analysis of the velocity and synchronicity of diaphragmatic motion: dynamic MRI in different postures. *Magn Reson Imaging*. 2006;24:1325–1332.
9. Kauczor H-U, Altes TA. *MRI of the Lung*. Verlag Berlin Heidelberg, Germany; Springer Science & Business Media; 2009.
10. Plathow C, Ley S, Fink C, et al. Evaluation of chest motion and volumetry during the breathing cycle by dynamic MRI in healthy subjects: comparison with pulmonary function tests. *Invest Radiol*. 2004;39:202–209.
11. Plathow C, Ley S, Fink C, et al. Analysis of intrathoracic tumor mobility during whole breathing cycle by dynamic MRI. *Int J Radiat Oncol Biol Phys*. 2004;59: 952–959.

12. Plathow C, Schoebinger M, Fink C, et al. Evaluation of lung volumetry using dynamic three-dimensional magnetic resonance imaging. *Invest Radiol*. 2005;40: 173–179.
13. Plathow C, Fink C, Sandner A, et al. Comparison of relative forced expiratory volume of one second with dynamic magnetic resonance imaging parameters in healthy subjects and patients with lung cancer. *J Magn Reson Imaging*. 2005; 21:212–218.
14. Blackall J, Ahmad S, Miquel M, et al. MRI-based measurements of respiratory motion variability and assessment of imaging strategies for radiotherapy planning. *Phys Med Biol*. 2006;51:4147–4169.
15. Tokuda J, Schmitt M, Sun Y, et al. Lung motion and volume measurement by dynamic 3D MRI using a 128-channel receiver coil. *Acad Radiol*. 2009; 16:22–27.
16. Griswold MA, Jakob PM, Heidemann RM, et al. Generalized autocalibrating partially parallel acquisitions (GRAPPA). *Magn Reson Med*. 2002;47:1202–1210.
17. Lingala SG, DiBella E, Adluru G, et al. Accelerating free breathing myocardial perfusion MRI using multi coil radial k-t SLR. *Phys Med Biol*. 2013;58: 7309–7327.
18. Lingala SG, Hu Y, DiBella E, et al. Accelerated dynamic MRI exploiting sparsity and low-rank structure: k-t SLR. *IEEE Trans Med Imaging*. 2011;30: 1042–1054.
19. Majumdar A, Ward RK. Causal dynamic MRI reconstruction via nuclear norm minimization. *Magn Reson Imaging*. 2012;30:1483–1494.
20. Majumdar A, Ward RK. Exploiting rank deficiency and transform domain sparsity for MR image reconstruction. *Magn Reson Imaging*. 2012;30:9–18.
21. Walsh DO, Gmitro AF, Marcellin MW. Adaptive reconstruction of phased array MR imagery. *Magn Reson Med*. 2000;43:682–690.
22. Lingala SG, Jacob M. Blind compressive sensing dynamic MRI. *IEEE Trans Med Imaging*. 2013;32:1132–1145.
23. Adluru G, McGann C, Speier P, et al. Acquisition and reconstruction of undersampled radial data for myocardial perfusion magnetic resonance imaging. *J Magn Reson Imaging*. 2009;29:466–473.
24. Liang ZP. Spatiotemporal imaging with partially separable functions. In *4th IEEE International Symposium on Biomedical Imaging: From Nano to Macro*. IEEE; 2007. ISBI 2007.988-991.
25. Lustig M, Santos JM, Donoho DL, et al. kt SPARSE: high frame rate dynamic MRI exploiting spatio-temporal sparsity. In: *Proceedings of the 13th Annual Meeting of International Society for Magnetic Resonance in Medicine (ISMRM), Seattle*. May 2006.
26. Otazo R, Kim D, Axel L, et al. Combination of compressed sensing and parallel imaging for highly accelerated first-pass cardiac perfusion MRI. *Magn Reson Med*. 2010;64:767–776.
27. Jung H, Park J, Yoo J, et al. Radial k-t FOCUSS for high-resolution cardiac cine MRI. *Magn Reson Med*. 2010;63:68–78.
28. Jung H, Sung K, Nayak KS, et al. k-t FOCUSS: A general compressed sensing framework for high resolution dynamic MRI. *Magn Reson Med*. 2009;61:103–116.
29. Bhave S, Lingala SG, Johnson CP, et al. Accelerated whole-brain multi-parameter mapping using blind compressed sensing. *Magn Reson Med* 2015.
30. Hansen PC, O'Leary DP. The use of the L-curve in the regularization of discrete ill-posed problems. *SIAM J Sci Comput*. 1993;14:1487–1503.
31. Ravishankar S, Bresler Y. MR image reconstruction from highly undersampled k-space data by dictionary learning. *IEEE Trans Med Imaging*. 2011;30: 1028–1041.
32. Sun D, Roth S, Black MJ. Secrets of optical flow estimation and their principles. In: *Conference on Computer Vision and Pattern Recognition (CVPR)*. San Fransisco, CA: IEEE; 2010. IEEE 2432-2439.
33. Dean E. Effect of body position on pulmonary function. *Phys Ther*. 1985;65: 613–618.
34. Moreno F, Lyons HA. Effect of body posture on lung volumes. *J Appl Physiol*. 1961;16:27–29.
35. Rom WN, Markowitz SB. *Environmental and Occupational Medicine*. Philadelphia, PA: Lippincott Williams & Wilkins; 2007.

APPENDIX A

Tradeoffs in Image Recovery Using Constrained Algorithms

The nuclear minimization scheme, the l_1 Fourier sparsity regularization scheme, and the BCS rely on modeling the temporal profiles/columns of the Casorati matrix. The sparsity priors on the coefficients $\mathbf{U}$ in BCS and on the Fourier coefficients in the l_1 Fourier sparsity regularization scheme cause many of the coefficients to be 0. Hence, these schemes use different basis functions at different pixels. The nuclear norm minimization scheme, in contrast, does not enforce any sparsity before and hence uses the same basis functions at each pixel. The projection of the intensity profile at the pixel (x, y), denoted by the vector $\widehat{\rho_{(x,y)}}$, is obtained as

$$\widehat{\rho_{(x,y)}} = \mathbf{P}_{(x,y)}\rho_{(x,y)},$$

where the matrix $\mathbf{P}_{(x,y)}$ is the specified by

$$\mathbf{P}_{(x,y)} = \mathbf{V}_{ac}^{'}\left(\mathbf{V}_{ac}\mathbf{V}_{ac}^{'}\right)^{-1}\mathbf{V}_{ac}. \quad (A.1)$$

The rows of the matrix $\mathbf{V}_{ac}$ are the temporal basis functions that are active at the pixel. The above relation shows that the intensity at the ith frame (ith row of $\hat{\rho}_{(x,y)}$) is obtained as the weighted linear combination of all the entries in $\rho_{(x,y)}$; the weights are specified by the ith row of $\mathbf{P}_{(x,y)}$. We term the rows of the $\mathbf{P}_{(x,y)}$ matrix in Eq. A.1 as the temporal point spread function (TPSF) because it characterizes averaging across time performed by the above-constrained schemes to remove aliasing, which is noiselike in case of radial undersampling (see Fig. A.1). We observe that each row of the matrix gives the weights for the corresponding time point.

Since we use the l_1 norm, which is a convex relaxation of l_0 sparsity, the recovered coefficients are not exactly sparse and have many small nonzero coefficients. Similarly, the recovered matrix is not exactly low rank in the nuclear norm setting. For visualization purposes, we truncate the coefficients whose magnitudes are less than 0.1% of the maximum in the Fourier sparsity regularization and BCS settings to generate Figure A.1. Similarly, we perform a singular value decomposition of the recovered matrix, followed by a truncation of singular values less than 0.1% of the maximum in the nuclear norm scheme. We stress that this truncation is used only for visualization; the actual algorithms do not use truncation. Figure A.1 shows the TPSF for 1 time point corresponding to peak inhalation (specified by solid orange line) obtained from the reconstructed data and the corresponding signal profiles at 3 pixels. The pixel intensity at a specific pixel and time point in the denoised image is obtained as a weighted linear combination of pixels at all the time points at the same spatial location; the weights are specified by the value of the TPSF. We observe that the TPSF values are higher for frames with similar respiratory phase (marked by dotted orange markers), which implies that these pixels contribute to the summation heavily. We observe that the TPSF is spatially and temporally varying for the BCS and l_1 Fourier sparsity regularization scheme. Because the low-rank minimization scheme uses the same set of basis functions at each pixel, in this case, the TPSF is only temporally varying. The TPSF for view-sharing method is both temporally and spatially invariant, as seen in Figure A.1.

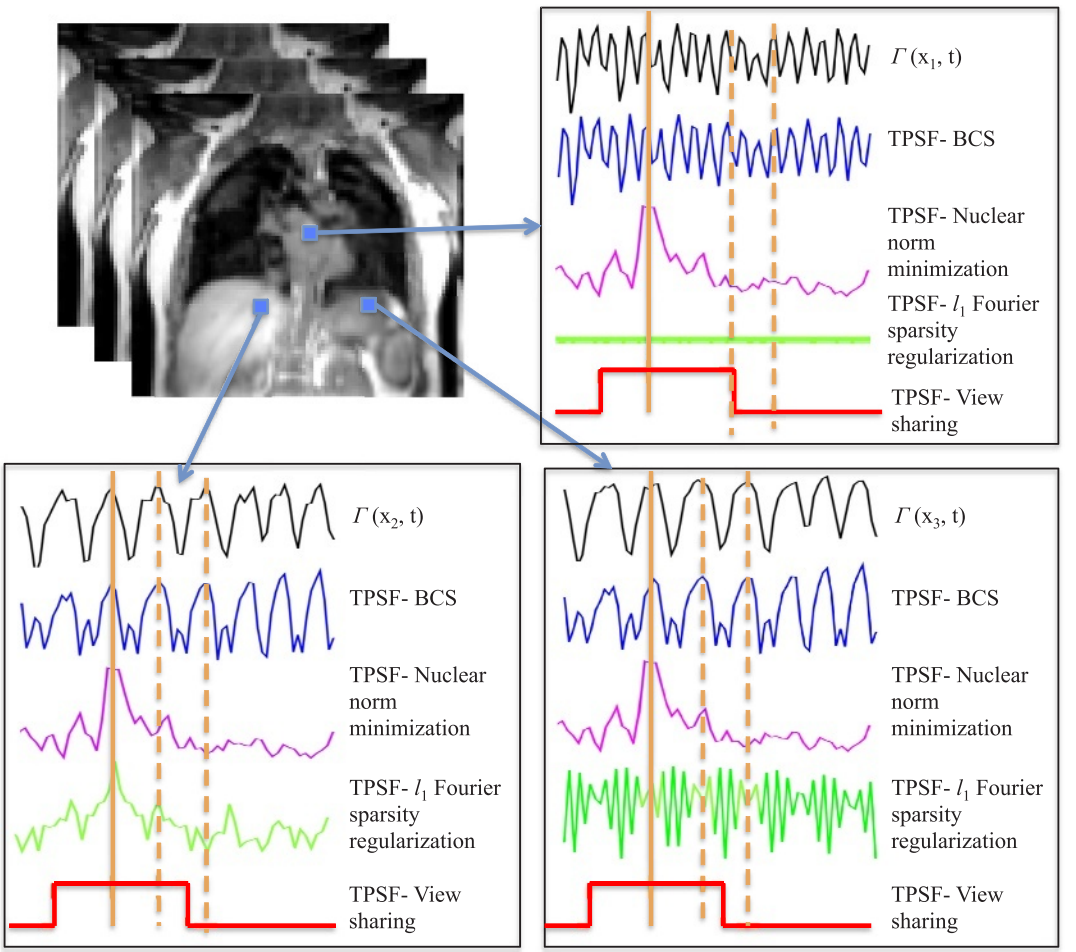

FIGURE A.1. Illustrations of different algorithms: The TPSFs at a specific timeframe at peak inhalation (shown by solid orange marker) and the underlying signal time profile are shown for 3 different pixels. The TPSF plots show that all the 3 constrained schemes provide nonlocal averaging of pixel values, thus offering good denoising without resulting in temporal blurring. However, the TPSF of view-sharing is spatially and temporally invariant and thus leads to significant temporal blurring. The TPSFs of the BCS and l_1 Fourier sparsity regularization schemes are spatially varying, whereas the nuclear norm minimization scheme is spatially invariant. We see that the TPSF from BCS is in good correlation with the underlying time profiles (black curves) at the respective pixels. The TPSF for the timeframes shown by the solid orange marker has high values corresponding to timeframes in the similar respiratory phase (shown by dotted orange marker). These frames contribute predominantly to the recovery of the specific frame because this recovery is a weighted combination of signal at other timeframes and the weights are specified by TPSF. Figure A.1. can be viewed online in color at www.investigativeradiology.com.